RESEARCH PAPER

Measurements of microbubble generation process in microchannel using ultra high-speed micro-PTV system

Mitsuhisa Ichiyanagi · Ryoji Miyazaki · Toshiyuki Ogasawara · Ikuya Kinefuchi · Yoichiro Matsumoto · Shu Takagi

Abstract Ultra high-speed micron-resolution particle tracking velocimetry (UH-µPTV) technique has been developed to advance the novel method to generate microbubbles using a T-shaped microchannel. The method can produce microbubbles with 10-µm order diameter by applying the gas pressure of several tens of kilopascal and injecting the deionized water with the speed of a few meters per second. The conventional µPTV was restricted to the velocity measurement of the order of millimeter per second due to a few kilohertz frame rate CMOS camera. On the other hand, the present UH-µPTV technique achieves to measure the liquid velocity of the order of meter per second by combining the bright-field microscopy and the ultra high-speed camera with 1 MHz frame rate. For improving the spatial resolution, the phase sampling method has been introduced and results in 10 velocity vectors in 20 µm × 20 µm area. The validation of the velocity measurement using UH-µPTV has been conducted through the comparison with the theoretical solution, and it has been shown that the proposed technique can capture the velocity vector field higher than 1 m/s. Furthermore, from the 1-µs time-series imaging, the microbubble generation process has been classified into two stages: the intruding stage and the growing stage. It has been shown that the bubble diameter becomes smaller by increasing the liquid velocity with reducing the period of the growing stage. In addition, from the velocity-vector maps, the normal components of velocities to the gas–liquid interface in the intruding stage are compared with those in the growing stage, and it has been observed that the velocity amplitudes in the growing stage are much larger than those in the intruding stage. This fact suggests that the high-speed liquid flow normal to the gas–liquid interface plays an important role in microbubble generation process.

M. Ichiyanagi
Department of Engineering and Applied Sciences,
Faculty of Science and Technology, Sophia University,
7-1 Kioi-cho, Chiyoda-ku, Tokyo 102-8554, Japan

R. Miyazaki · I. Kinefuchi · Y. Matsumoto · S. Takagi (✉)
Department of Mechanical Engineering, Graduate School
of Engineering, The University of Tokyo, 7-3-1 Hongo,
Bunkyo-ku, Tokyo 113-8656, Japan
e-mail: takagi@mech.t.u-tokyo.ac.jp

T. Ogasawara
Department of Mechanical Engineering, Graduate School
of Engineering, Osaka Prefecture University, 1-1 Gakuen-cho,
Naka-ku, Sakai, Osaka 599-8531, Japan

1 Introduction

Microbubbles are widely used for biological and medical applications, e.g., a contrast agent for ultrasonic diagnosis (Goldberg et al. 1994) and ultrasound-guided drug delivery systems (Soetanto and Watarai 2000; Ferrara et al. 2007), because their ultrasonic scattering property is excellent in comparison with other contrast agents. In particular, monodisperse bubbles with the diameter of less than 5 µm are required for the well-defined frequency response to ultrasound and the capability of entering through blood capillaries. One of the methods to generate microbubbles is the unique technique using a T-shaped microchannel (Günther and Jensen 2006; Garstecki et al. 2006; Xu et al. 2006). This technique gives 10-µm order diameter bubbles by applying the gas pressure of tens of kilopascal and

injecting the deionized water with the speed of 1 m/s. The advantages of this technique are the uniformity of bubble diameter and the high generation frequency in the order of 10^5 bubbles per second. However, it is difficult to generate several micrometers diameter bubbles. For the production of smaller microbubbles, it is necessary to investigate the dynamics of microbubble generation in a T-shaped microchannel by developing the novel velocity measurement technique with a high time resolution. The required performances are to capture the velocity field of approximately 1 m/s with the time-series measurement of more than 10^6 Hz and to visualize the bubble generation process simultaneously.

Santiago et al. (1998) developed a micron-resolution particle image velocimetry (μPIV) technique using fluorescent particles, an epifluorescent microscopy and a digital CCD camera with the frame rate of the order of 10 Hz. They applied this technique to a Hele-Shaw flow around a 30-μm elliptical cylinder, and obtained a two-dimensional and two-component velocity distribution of approximately 50 μm/s. Meinhart et al. (1999) improved the μPIV system using a double-pulsed Nd: YAG laser with time interval of 500 ns, and this measured the velocity field of the order of millimeter per second in a straight microchannel. Yan et al. (2006) increased the time resolution to 2×10^3 Hz by applying a phase sampling technique and obtained the velocity profiles in a transient electroosmotic flow. This advanced technique is, however, applicable only to a periodic flow. Ichiyanagi et al. (2007, 2009, 2012) applied the confocal microscopy to the μPIV system, instead of the epifluorescent microscopy, and the depthwise velocity was evaluated using the continuity equation. This system yields the three-dimensional and three-component velocity distribution. These above-mentioned works were, however, limited to the velocity measurement of a few millimeters per second and the low time resolution of the order of 10^1–10^3 Hz due to the use of a CCD camera. Recently, a digital CMOS camera with the frame rate of a few kilohertz was adopted for the μPIV system, and the two-dimensional and two-component velocity distributions of a few millimeters per second were obtained with the time resolution of 10^3 Hz. This system is applicable even for nonperiodic flows in contrast to the conventional systems with a CCD camera. The μPIV system with a CMOS camera was applied to the velocity measurement in microfluidic devices (Shinohara et al. 2004; Senga et al. 2010) and in in vitro and in vivo blood flows (Sugii et al. 2005; Jeong et al. 2006). Kazoe et al. (2010) proceeded to the three-dimensional and three-component velocity measurements using the continuity equation. van Steijn et al. (2007) and Xiong et al. (2007) measured liquid velocity distributions in a bubble generation process using a T-shaped and straight-shaped microchannel, respectively. Their bubble diameters were ranging from 0.1 mm to 1 mm,

and the averaged velocity was of the order of 10 mm/s. Furthermore, previous works of various velocity measurements using μPIV were reviewed by Sinton (2004), Lindken et al. (2009) and Wereley and Meinhart (2010). However, nobody so far succeeded to measure the velocity field of a few meters per second with a time resolution of more than 10^6 Hz and visualized the bubble generation process simultaneously.

The objectives of the present study are to develop a high time-resolved velocity measurement technique with simultaneous visualization of the gas–liquid interface in a microchannel and obtain a strategy for generating further smaller diameter bubbles in T-shaped microchannels. The measurement system is based on a bright-field microscopy equipped with a 1×10^6 frames/s recordable ultra high-speed camera. The bright-field microscopy has the ability to visualize the interface between the gas and liquid phases and to project particles as the shadowgraph, and thus, this system is able to obtain the particle and bubble images simultaneously. The present technique is validated by comparing the velocity distribution with the theoretical solution. The proposed technique is successful to obtain the 1-μs time-series velocity vectors of a few meters per second in a liquid phase around microbubbles and to observe the microbubble generation process.

2 Measurement technique

2.1 Overview of velocity measurement technique

Micron-resolution particle image velocimetry (μPIV) or micron-resolution particle tracking velocimetry (μPTV) techniques have been widely used to investigate velocity fields in microchannel flows. These techniques require seeding tracer particles with a diameter ranging from 0.1 μm to a few micrometers, and velocity distributions are obtained through the information of particle motion with various particle tracking algorithms. The effect of the Brownian motion on the velocity measurement can be eliminated by the ensemble-averaging technique (Santiago et al. 1998). These optical measurement systems are based on the epifluorescent microscopy with a digital CCD or CMOS camera. In general, the particle diameter is close to the diffraction limit, so that the fluorescent particles are employed as the tracer particles, because their fluorescent images are larger than the scattered light images. However, these systems are only applicable to velocity measurements of the order of millimeter per second since the weak intensity of the fluorescence restricts the frame rate for capturing particle images up to a few kHz.

In this study, we propose the novel measurement technique, which is referred as ultra high-speed μPTV (UH-μPTV), to

measure the velocity fields of a few meters per second with the time-series measurement of up to 10^6 Hz and to visualize an interfacial shape during microbubble generation process simultaneously. The system is composed of an ultra high-speed camera with 1×10^6 frames/s and the bright-field microscopy, which can capture particle images and gas–liquid interfaces as the shadowgraph. Furthermore, the bright-field microscopy gives the lower limit of the particle diameter, which is approximately 1 μm in the present study, due to the diffraction limit. In order to prevent the clogging of microchannels, we adopted the low concentration of tracer particles, which leads to the low spatial resolution of velocity measurements. For the improvement of the spatial resolution, the μPTV technique with the phase sampling method (Sugii et al. 2000; Yan et al. 2006; Kazoe et al. 2010) was applied. The relative error due to the Brownian motion, ε_B, is estimated by the following equation (Santiago et al. 1998):

$$\varepsilon_B = \frac{1}{u}\sqrt{\frac{2D}{\Delta t}}, \text{ where } D = \frac{\kappa T}{3\pi\mu d_p} \tag{1}$$

where u (m/s) is the streamwise velocity, Δt (s) is the time interval of the camera frame, κ ($m^2 kg/s^2 K$) is Boltzmann constant, T (K) is the absolute temperature of the fluid, μ ($kg\ s/m^2$) is the viscosity of the fluid and d_p (m) is the particle diameter. In the present study, the above-mentioned relative error was evaluated to be approximately 0.01 %, and thus, the effect of the Brownian motion on the velocity detection was negligibly small and the ensemble-averaging technique was not applied to the proposed velocity measurement technique. In addition, in the present UH-μPTV technique, hierarchical processing was employed based on cross-correlation and the sub-pixel analysis was achieved by fitting the correlation coefficient to a Gaussian distribution (Westerweel 1997). Using this method, the measurement uncertainty was found to be 0.03 m/s at 95 % confidence level.

2.2 Measurement system and microchannel

Figure 1 illustrates a schematic of the optical measurement system comprising an inverted microscope (Nikon Corp., Eclipse Ti-U), a continuous mercury lamp operating at a power of 100 W (OSRAM GmbH., HBO103 W/2 N), an oil immersion 60× magnification objective lens with a numerical aperture of 1.4 (Nikon Corp., CFI Plan Apo) and an ultra high-speed camera (Shimadzu Corp., HyperVision HPV-1, 312×260 pixels, 30 frames/s—1×10^6 frames/s). This setup covered a measurement area of 350×290 μm. For the comparison between the bright-field microscopy and epifluorescent microscopy, the measurement area was illuminated by the mercury lamp from the upper side and the bottom side of the microchannel, respectively. The increased temperature
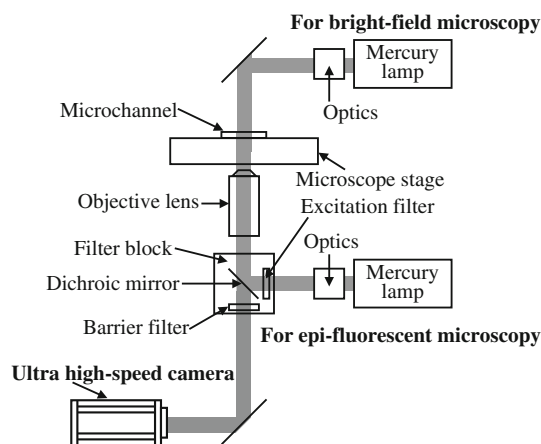

Fig. 1 Schematic of optical measurement system

due to the illumination of the mercury lamp was estimated to be less than 1 K, so that the photothermal effect is considered to be negligible.

Figure 2 shows the schematic diagram of a T-shaped microchannel (Institute of Microchemical Technology Co., Ltd.) which was made of borosilicate glass and fabricated by the wet etching process. The channel width and depth at the T-junction area were 110 and 20 μm, respectively. The gas phase was provided from the upper channel named as the orthogonal channel. The inlet and outlet of the liquid phase are located at the left and the right side of the microchannel, respectively. We designed the channel width of the liquid phase larger at both upstream and downstream of the T-junction area. This enabled us the increase of the liquid flow velocity at the T-junction area without causing the drastic increase of the pressure loss. In addition, a straight-shaped microchannel with the width and depth of 100 and 20 μm was fabricated for the validation of the UH-μPTV technique through the comparison of velocity distribution between the experimental results and the theoretical solution.

2.3 Gas and liquid flow conditions

Fluorescent polystyrene particles (1.0 μm in diameter; Invitrogen Corp., FluoSpheres F8823) were employed as tracer particles for UH-μPTV, which were added to the ultrapure water at a volume fraction of 0.04 %. Peak values for the absorption and emission fluorescence wavelengths were 505 nm and 515 nm, respectively. The water with particles was injected into the bottom-left microchannel (Fig. 2) with the flow rate of 70–200 μL/min controlled by the syringe pump (KD Scientific Inc., KDS210), whose average liquid velocity was 0.6–1.6 m/s. For the gas phase, nitrogen (N_2) was used and supplied to the top-left microchannel in Fig. 2. The gas flow was controlled at a
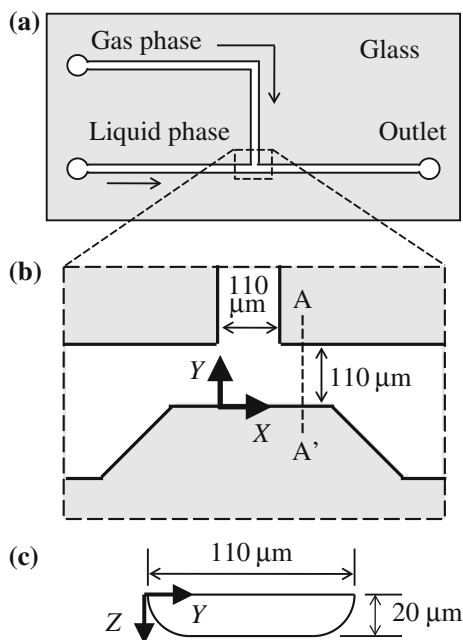
Fig. 2 **a** Top view of T-shaped microchannel and **b** measurement area. **c** Cross-sectional view along the A–A'

constant pressure of 55 kPa using a regulator and a pressure controller (Nagano Keiki Co., Ltd., PC20).

3 Results and discussion

3.1 Comparison between epifluorescent microscopy and bright-field microscopy

The bubble generation processes in the T-shaped microchannel were visualized using the measurement system with the epifluorescent microscopy and that with the bright-field microscopy. Their instantaneous images are shown in Figs. 3 and 4, respectively. The experimental conditions in both images were set at the gas pressure of 55 kPa and the average liquid velocity of 0.74 m/s. The exposure times of the camera for Figs. 3 and 4 were set to 1 ms (i.e., the frame rate of 1×10^3 frames/s) and 4 μs (i.e., the frame rate of 2.5×10^5 frames/s), respectively, because these setups produce the high signal-to-noise (S/N) ratio. The S/N ratios of both images were evaluated to be 3.8 and 2.3, respectively, which are sufficiently high to apply μPIV or μPTV (Kazoe et al. 2010). For the epifluorescent microscopy, the white lines indicate trajectories of fluorescent particles, and the black color region corresponds to both the gas phase and background image. Since the particle images indicate the path lines, it is difficult to apply the μPTV algorithm and obtain the velocity information. On the other hand, for the bright-field microscopy, the tracer particles and the interfaces between the gas and
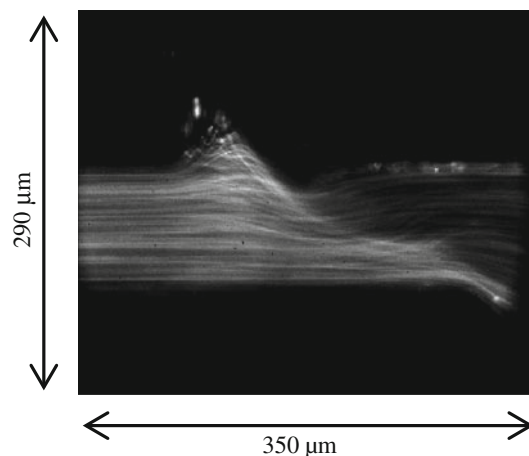

Fig. 3 Instantaneous image obtained by the measurement system using epifluorescent microscopy and the camera with 1 kHz frame rate. *White lines* indicate the path lines of fluorescent tracer particles
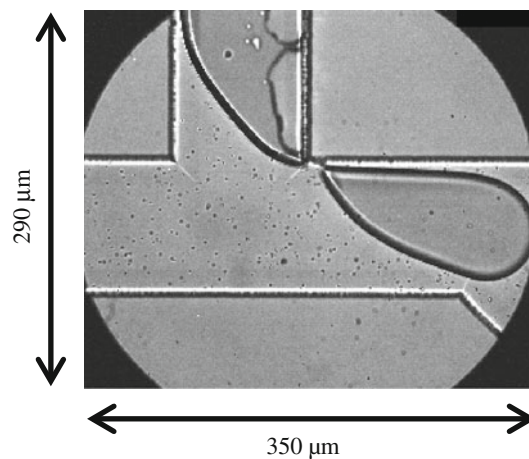

Fig. 4 Instantaneous image obtained by the measurement system using bright-field microscopy and the camera with 250 kHz frame rate. *Black points* and *lines* indicate tracer particles and the interface between gas and liquid phases, respectively

liquid phases are represented as the black points and lines, respectively, by the shadowgraph method. The bright-field microscopy is able to capture both particle and bubble images with the high time resolution. This feature enables us the simultaneous measurement of the motion of the gas–liquid interface and the velocity field in the liquid phase during the generation process of microbubbles.

Furthermore, the depth resolution of the epifluorescent microscopy is estimated to 3.1 μm, because the out-of-focus particle image is cutoff using the image processing and only the in-focus particle image is used to apply μPIV or μPTV (Meinhart et al. 2000). Its cutoff threshold is defined as a tenth of the intensity of the in-focus particle image. On the other hand, the depth resolution of the bright-field microscopy is the same as the channel depth (20 μm in this study), because the intensities of all the

particle images in the depthwise direction have almost the same values and we cannot distinguish them in the in-focus and out-of-focus planes by the image processing. This leads to the reduction of spatial resolution in the depthwise direction.

3.2 Validation of velocity measurement

The velocity measurement using UH-μPTV with the phase sampling method was validated through the comparison of a liquid velocity distribution in the straight-shaped microchannel with the theoretical solution (White 2006). The experiment was conducted by regulating the average liquid velocity at approximately 0.6 m/s, which corresponds to the flow rate of 70 μL/min and the Reynolds number of 20. Figure 5a shows the instantaneous velocity-vector map obtained by UH-μPTV, and it is illustrated that the vectors are unevenly distributed and their number is approximately 200 in the area of 300 × 100 μm. On the other hand, Fig. 5b exhibits the velocity-vector map using UH-μPTV with the phase sampling method. This map is given by integrating five instantaneous velocity-vector maps. With this superimposition, a sufficient number of velocity vectors are acquired at whole the measurement area to analyze the local flow structure. For further validation of this technique in detail, the streamwise velocities by UH-μPTV are plotted in Fig. 6. The trapezoidal curves show the maximum and average velocity distributions of the theoretical solution of the Hagen–Poiseuille flow in the straight-shaped microchannel (White 2006):

$$u(y,z) = \frac{16a^2}{\mu\pi^3}\left(-\frac{dp}{dx}\right)$$
$$\sum_{n=1,3,5,...}^{\infty}(-1)^{(n-1)/2}\left[1-\frac{\cosh(n\pi z/2a)}{\cosh(n\pi b/2a)}\right]\frac{\cos(n\pi y/2a)}{n^3} \quad (2)$$
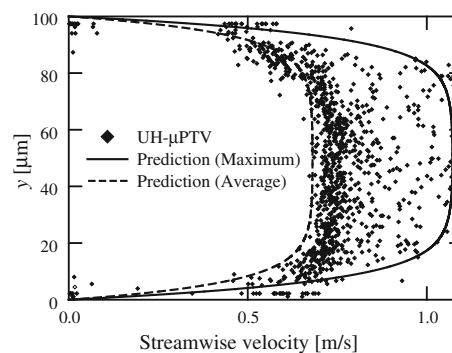
Fig. 6 Streamwise velocity obtained by UH-μPTV with the phase sampling method in straight microchannel. The *trapezoidal curves* show the maximum and average velocity profile based on Hagen–Poiseuille flow in straight microchannel

where, a (m) is the half width of the microchannel, b (m) is the half depth and dp/dx (Pa/m) is the pressure gradient. In the present study, a and b were 50 and 10 μm, respectively. As shown in Fig. 6, the particle velocities are located between the average velocity and the maximum velocity of the theory. This was caused by the lack of the spatial resolution in the depthwise direction due to the bright-field microscopy. Although this point is the shortcoming in this technique, except this point, it should be noted that the present UH-μPTV has been able to capture the velocity vectors of approximately 1 m/s.

3.3 Effect of average liquid velocity on formation frequency of microbubbles

Figure 7 shows the time-series instantaneous images of the bubble generation process in the T-shaped microchannel captured with a frame rate of 5×10^5 Hz. This experiment was conducted under the condition of the gas pressure of 55 kPa and the average liquid velocity of 1.0 m/s and resulted in the periodic bubble formation at a frequency of $1/T = 1 \times 10^4$ Hz. It was observed at the downstream corner of orthogonal channel that the gas phase is coming out into the main channel (first stage, $0 < t < 30$ μs), and is squeezed and consequently broken up at the corner between the orthogonal stream and downstream (second stage, 30 μs $< t < 100$ μs). In the present study, the bubble generation process is divided into the above two stages, which are hereinafter referred to as the intruding stage and the growing stage, respectively. Figure 8 illustrates the definition of these stages. The intruding stage is defined as the initial part of the bubble growth process before the tip part of the microbubble gets passing through the extended line of the orthogonal channel wall (illustrated as the dashed line in Fig. 8). The successive growing stage is until the growing microbubble is finally pinched off at the corner of the T-junction. Figure 9a illustrates the relationship between
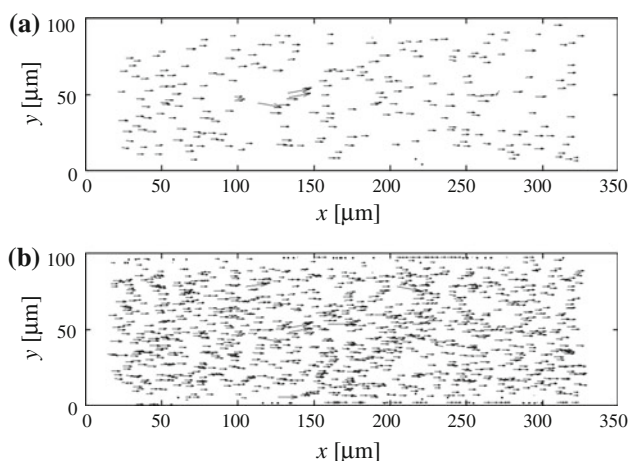
Fig. 5 Velocity-vector maps obtained by using **a** UH-μPTV and **b** UH-μPTV with the phase sampling method in straight microchannel
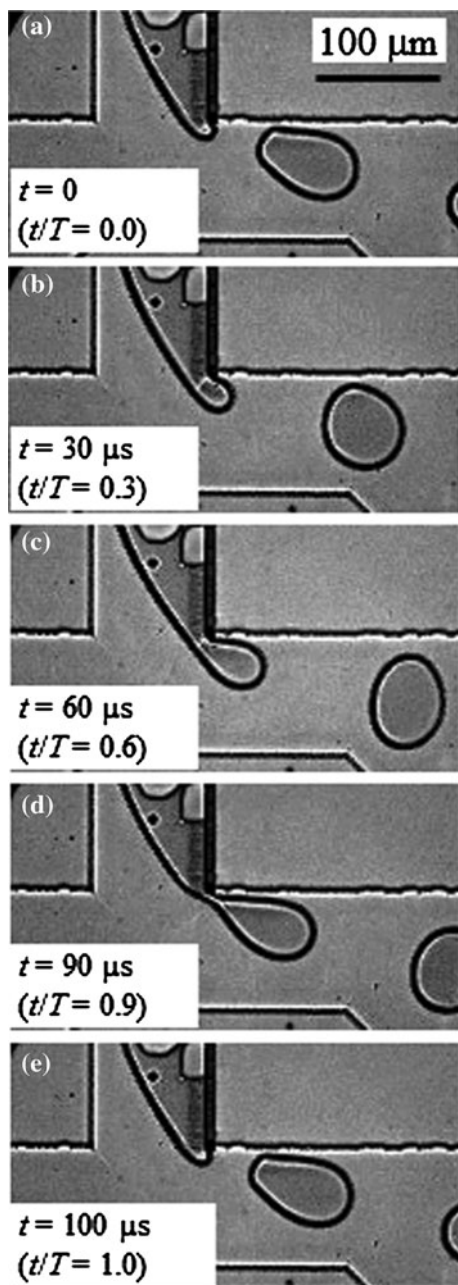
Fig. 7 Time-series instantaneous images of microbubble generation process obtained by the measurement system using bright-field microscopy and the camera with 500 kHz frame rate. The experiments were conducted under the conditions with the gas pressure of 55 kPa and the average liquid velocity of 1.0 m/s

Fig. 8 Definition of **a** the intruding stage and **b** the growing stage of microbubble generation process

Fig. 9 **a** Relationship between period of microbubble formation and average liquid velocity. **b** Period of intruding and growing stages as a function of the average liquid velocity

the period of bubble formation T, and the average liquid velocity. In Fig. 9b, the period of the intruding stage is compared with that of the growing stage. The experiments were performed under the conditions of the gas pressure of 55 kPa and the average liquid velocities of 0.6–1.5 m/s. The period of bubble formation has a minimum at a certain velocity of the liquid phase. This is caused by the competition between the increase in the period of the intruding
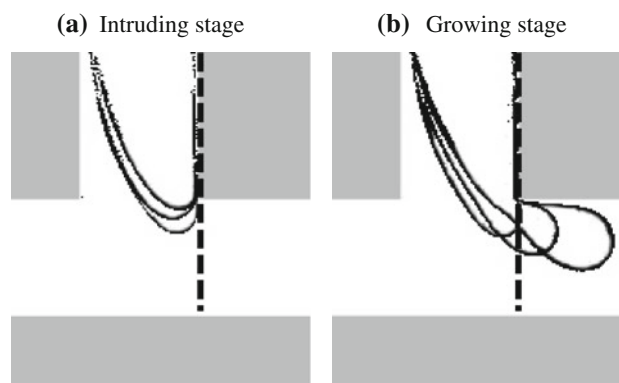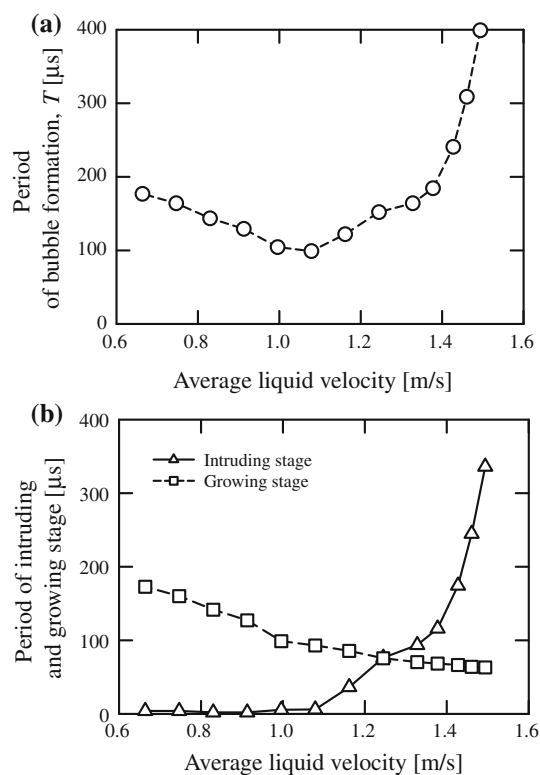
stage and the decrease in that of the growing stage for the larger liquid velocity. The larger liquid velocity prevents the motion of the gas–liquid interface in the orthogonal channel and, as a consequence, increases the period of the intruding stage. On the other hand, the period of the growing stage becomes shorter for the larger liquid velocity because of the larger pinch-off force to the growing bubble as discussed in Sect. 3.5. The shortest period of the growing

stage realized in our experiment was in the order of 10 μs. To the best of our knowledge, the measurement of such fast phenomena in microchannel flows has become possible for the first time, by introducing the present UH-μPTV system with the maximum time resolution of 1 μs.

3.4 Effect of average liquid velocity on microbubble diameter

The effect of the average liquid velocity on the bubble diameter was investigated under the same experimental conditions in Fig. 9, and the typical images are represented in Fig. 10. It is qualitatively illustrated that the bubble diameter becomes smaller with an increase in the liquid velocity at the constant gas pressure. For the quantitative evaluation, the bubble diameters were estimated by calculating the bubble areas in the captured images and evaluating the equivalent diameter: diameter of the same volume sphere. Figure 11 exhibits the relationship between the bubble diameter and the average liquid velocity. The bubble diameters were evaluated by averaging five measurements, and the error bars indicate the standard
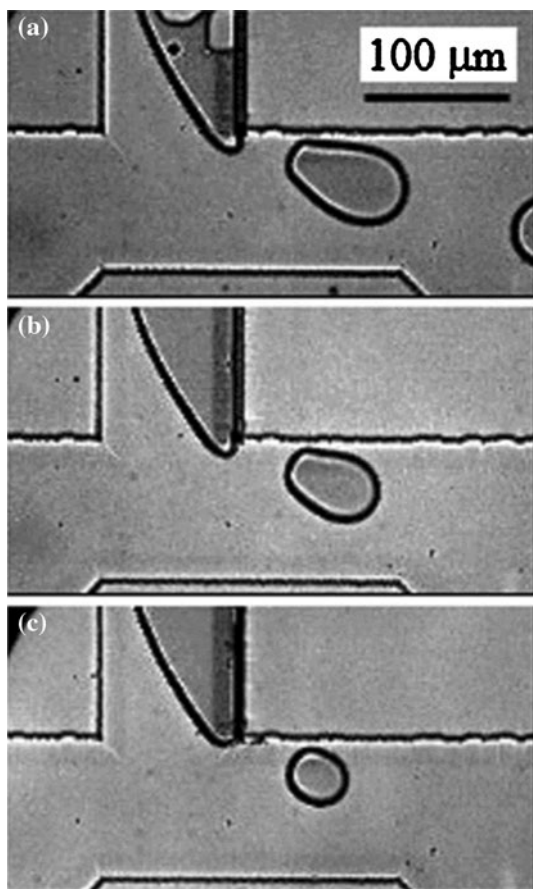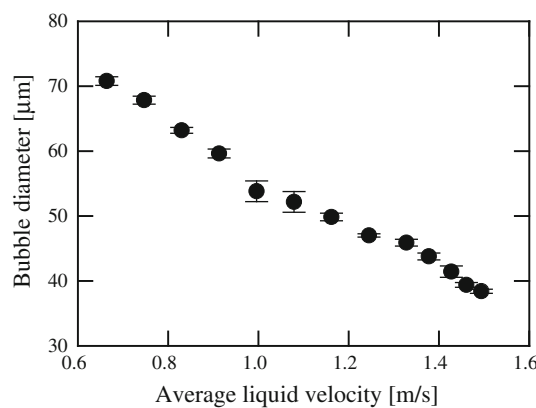

Fig. 11 Relationship between microbubble diameter and average liquid velocity. The experiments were conducted under the conditions with the constant gas pressure of 55 kPa. The *error bars* indicate the standard deviations of bubble diameter measurements

deviations. The ratio between the standard deviation and the bubble diameter was 1.3 % on average, and this result indicates that the bubble diameter is regarded to be uniform under the same experimental conditions. The bubble diameter decreases from 70 to 40 μm with increasing the average liquid velocity from 0.6 m/s to 1.5 m/s. In the previous section, as shown in Fig. 9b, an increase in the average liquid velocity leads to the increase in the period of intruding stage and the decrease in that of growing stage. As shown in Fig. 10, the shape of the gas–liquid interface at the end of the intruding stage shows rather weak dependence on the liquid velocity. Thus, the bubble diameter is determined mainly by the period of the growing stage, whereas the effect of the intruding stage is less dominant. These facts suggest that the bubble diameter becomes smaller by increasing the liquid velocity and reducing the period of growing stage. However, under the condition of the average liquid velocity larger than 1.6 m/s with the gas pressure of 55 kPa, it was observed that the gas phase is kept rest in the orthogonal channel, and the microbubble is not generated. This indicates that the upper limit of liquid velocity and the lower limit of generated bubble diameter exist under the constant gas pressure condition. In order to generate smaller bubbles, it is important to investigate the detailed mechanical characteristics between the gas and liquid phases during the squeezing and breaking-up process of gas phase for the reduction of the period of growing stage.

3.5 Velocity-vector field of microbubble generation process

For further investigation of the mechanism of bubble generation, the time-series images with the velocity vectors during one period of bubble formation were obtained using

Fig. 10 Instantaneous images of microbubble generation with the gas pressure of 55 kPa and the average liquid velocity of **a** 1.0 m/s, **b** 1.2 m/s and **c** 1.5 m/s
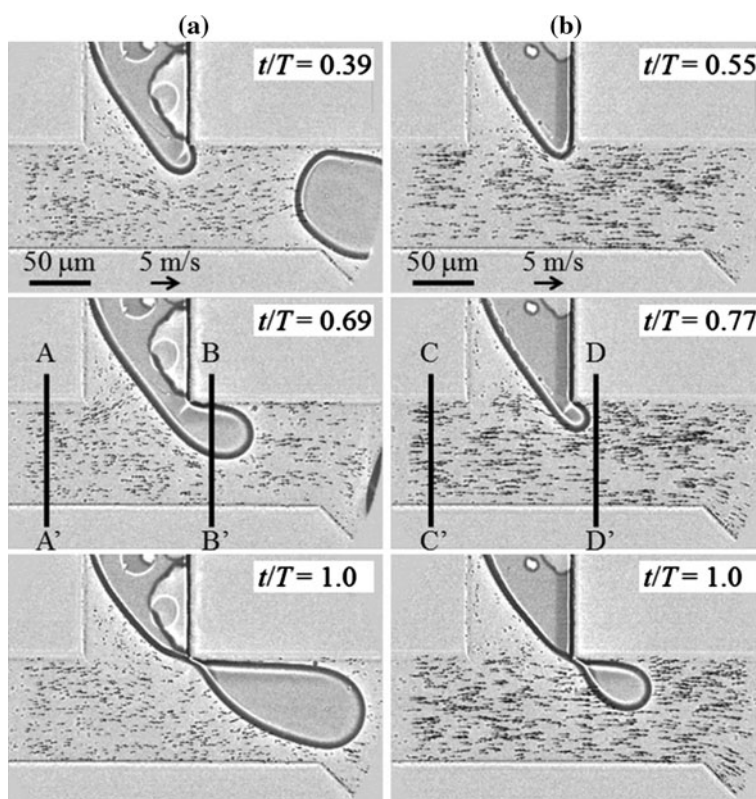
Fig. 12 Time-series instantaneous images with velocity-vectors in liquid phase obtained by using UH-µPTV with the phase sampling method. The experiments were performed under the conditions with the gas pressure of 55 kPa and the average liquid velocity of **a** 0.74 m/s and **b** 1.5 m/s

UH-µPTV with the phase sampling method. The results are shown in Fig. 12. These maps are given by integrating 6–8 instantaneous velocity-vector maps, and approximately 1,000 vectors are shown at the measurement area, which correspond to 10 vectors on average in the area of 20×20 µm. These results indicate that the proposed technique is able to capture the time-series velocity vectors of 2–3 m/s in a liquid phase around microbubbles and the interfacial shape in the generation process of approximately 10,000 microbubbles per second simultaneously. Figure 12a illustrates the velocity-vector maps under the average liquid velocity of 0.74 m/s, and Fig. 12b does the liquid velocity of 1.5 m/s, which is close condition of the upper limit of the bubble generation. From Fig. 12a and b, it is shown that the liquid flow is partially blocked by the bubble growth in the downstream of the main channel and the velocity vectors are directed toward the perpendicular to the gas–liquid interface around the corner of the orthogonal channel and the main channel.

For the quantitative evaluation of the relationship between the bubble growth and the liquid flow velocity, the flow rates across the cross-sections along A–A', B–B', C–C' and D–D' in Fig. 12 were roughly estimated from the velocity-vector map, and their values are 90 ± 5 µL/min, 45 ± 5 µL/min, 185 ± 15 µL/min and 145 ± 15 µL/min, respectively. The maximum estimates of the flow rate difference between A–A' and B–B', and between C–C'

and D–D' are 55 and 70 µL/min. This fact suggests that the bubble growth reduces the liquid flow rate at the downstream. Furthermore, the areas of the liquid phase in the orthogonal channel deduced from Fig. 12a and b are increasing at a rate of 100 ± 20 µm^2 per 1 µs and 220 ± 40 µm^2 per 1 µs. These rates correspond to the flow rates of 40 ± 5 µL/min and 80 ± 10 µL/min, which are in reasonable agreement with the flow rates difference between the downstream and the upstream. Thus, it is suggested that the bubble growth gives rise to the decrease in the liquid flow rate into the downstream and the corresponding increase in the liquid flow into the orthogonal stream.

The effect of the liquid flow velocity on the bubble generation process was further investigated using the zoom images around the corner between the orthogonal stream and downstream in Fig. 12. Figure 13 shows the instantaneous images with the velocity vectors of normal components to the gas–liquid interface, and Fig. 14 summarizes the histograms of normal components of velocities shown in Fig. 13. It is illustrated in Fig. 14a and b that the velocities in the growing stage are larger than those in the intruding stage. This is attributed to the increase in the liquid flow into the orthogonal stream, which is accompanied with the bubble growth in the downstream. Hence, this normal component of the liquid velocity toward the gas–liquid interface governs the transition from the

Fig. 13 Magnified images around the corner between the main and the orthogonal channels with velocity vectors of normal component to the gas–liquid interface obtained by UH-μPTV with the phase sampling method. The experiments were conducted under the conditions with the gas pressure of 55 kPa and the average liquid velocity of **a** 0.74 m/s and **b** 1.5 m/s

(a)

(b)

→

1 m/s

$t/T = 0.27$ (Intruding stage)

$t/T = 0.81$ (Intruding stage)

$t/T = 0.69$ (Growing stage)

$t/T = 0.89$ (Growing stage)

Fig. 14 Histograms of normal component of velocity to the interface between gas and liquid phases obtained by UH-μPTV with the phase sampling method. The experiments were conducted under the conditions with the gas pressure of 55 kPa and the average liquid velocity of **a** 0.74 m/s and **b** 1.5 m/s
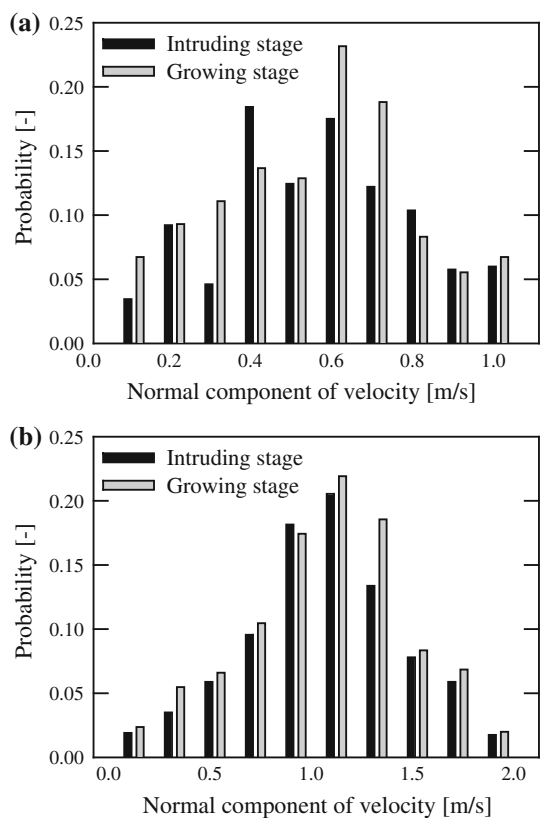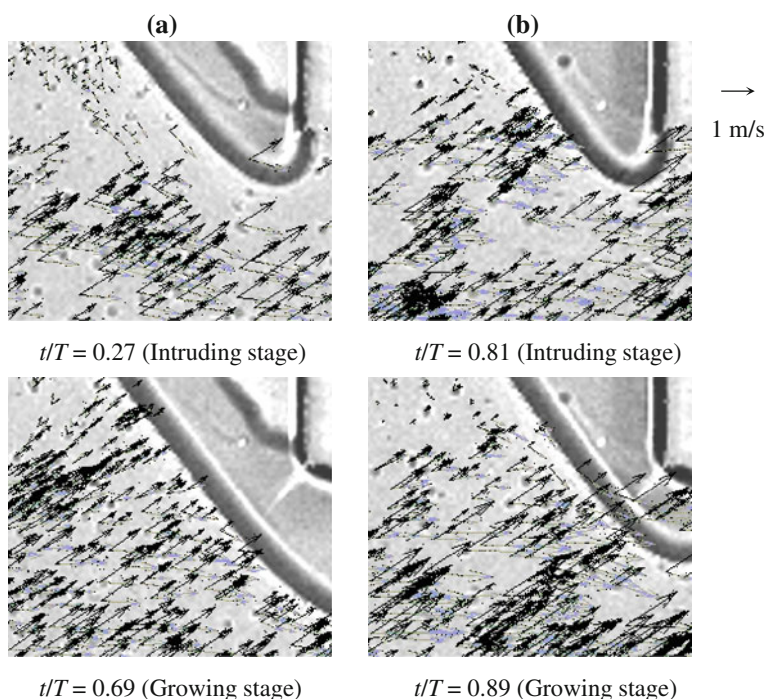
intruding stage to the growing stage and is likely to contribute to the force related to the pinching off and finally to a decision of generated bubble size.

4 Conclusions

UH-μPTV was developed by combining the bright-field microscopy and the ultra high-speed camera with 1×10^6 frames/s, for investigating the microbubble generation process in a microchannel. The present technique achieved to measure the 1 μs time-series liquid velocity of a few meters per second and to visualize the generation process of approximately 10,000 bubbles per second simultaneously. For improving the spatial resolution, the phase sampling method was introduced and resulted in 10 vectors in $20 \times 20 \ \mu m^2$ by integrating 6–8 instantaneous velocity-vector maps.

The validation of UH-μPTV with the phase sampling method was conducted by measuring a liquid velocity distribution in the straight-shaped microchannel and comparing it with the theoretical one. The advantage of the present method is the capability of detecting the velocity amplitude of approximately 1 m/s, which is not able to be captured using the conventional μPIV system.

The bubble generation process was visualized using 1 μs time-series imaging technique, and it was shown that the process is classified into the intruding stage and the growing stage, whose total time cycle is raging from 10-μs order to 100-μs order in our experimental conditions. The period of growing stage decreases with increasing the

liquid velocity under the constant gas pressure condition. Furthermore, the effect of the liquid velocity on the bubble diameter was evaluated by calculating the bubble areas in the captured images, and it was shown that the bubble diameter becomes smaller with an increase in the liquid velocity.

The effect of the liquid flow on the bubble generation process was discussed using the velocity-vector maps in a liquid phase around microbubbles and calculating the liquid flow rates at the upstream and downstream of the main channel. It was observed that the bubble growth leads to the decrease in the flow rate into the downstream and the increase in the flow rate into the orthogonal channel, and that the flow normal to the gas–liquid interface plays an important role in bubble generation process. The knowledge obtained from this study provides a strategy for generating further smaller diameter bubbles in T-shaped microchannels.

References

Ferrara K, Pollard R, Borden M (2007) Ultrasound microbubble contrast agents: fundamentals and application to gene and drug delivery. Annu Rev Biomed Eng 9:415–447

Garstecki P, Fuerstman MJ, Stone HA, Whitesides GM (2006) Formation of droplets and bubbles in a microfluidic T-junction - scaling and mechanism of break-up. Lab Chip 6:437–446

Goldberg BB, Liu JB, Forsberg F (1994) Ultrasound contrast agents: a review. Ultrasound in Med Biol 20(4):319–333

Günther A, Jensen KF (2006) Multiphase microfluidics: from flow characteristics to chemical and materials synthesis. Lab Chip 6:1487–1503

Ichiyanagi M, Sato Y, Hishida K (2007) Optically sliced measurement of velocity and pH distribution in microchannel. Exp Fluids 43:425–435

Ichiyanagi M, Sasaki S, Sato Y, Hishida K (2009) Micro-PIV/LIF measurements on electrokinetically-driven flow in surface modified microchannels. J Micromech Microeng 19: 045021

Ichiyanagi M, Tsutsui I, Kakinuma Y, Sato Y, Hishida K (2012) Three-dimensional measurement of gas dissolution process in gas-liquid microchannel flow. Int J Heat Mass Trans 55:2872–2878

Jeong JH, Sugii Y, Minamiyama M, Okamoto K (2006) Measurement of RBC deformation and velocity in capillaries in vivo. Microvasc Res 71:212–217

Kazoe Y, Nakamura T, Sato Y (2010) Evanescent-wave/volume illuminated velocity measurements of transient electrokinetically driven flow with nonuniform wall electrostatic potential. Meas Sci Technol 21: 055401

Lindken R, Rossi M, Große S, Westerweel J (2009) Micro-particle image velocimetry (μPIV): recent developments, applications, and guidelines. Lab Chip 9:2551–2567

Meinhart CD, Wereley ST, Santiago JG (1999) PIV measurements of a microchannel flow Exp Fluids 27:414–419

Meinhart CD, Wereley ST, Gray MHB (2000) Volume illumination for two-dimensional particle image velocimetry. Meas Sci Technol 11:809–814

Santiago JG, Wereley ST, Meinhart CD, Beebe DJ, Adrian RJ (1998) A particle image velocimetry system for microfluidics. Exp Fluids 25:316–319

Senga Y, Nakamura T, Fukumura H, Ichiyanagi M, Sato Y (2010) Near-wall motion of caged fluorescent dye in microchannel flows obtained from evanescent wave molecular tagging. J Fluid Sci Technol 5(2):192–206

Shinohara K, Sugii Y, Aota A, Hibara A, Tokeshi M, Kitamori T, Okamoto K (2004) High-speed micro-PIV measurements of transient flow in microfluidic devices. Meas Sci Technol 15: 1965–1970

Sinton D (2004) Microscale flow visualization. Microfluid Nanofluid 1:2–21

Soetanto K, Watarai H (2000) Development of magnetic microbubbles for drug delivery system (DDS). Jpn J Appl Phys 39:3230–3232

Sugii Y, Nishio S, Okuno T, Okamoto K (2000) A highly accurate iterative PIV technique using a gradient method. Meas Sci Technol 11:1666–1673

Sugii Y, Okuda R, Okamoto K, Madarame H (2005) Velocity measurement of both red blood cells and plasma of in vitro blood flow using high-speed micro PIV technique. Meas Sci Technol 16:1126–1130

van Steijn V, Kreutzer MT, Kleijn CR (2007) μ-PIV study of the formation of segmented flow in microfluidic T-junctions. Chem Eng Sci 62:7505–7514

Wereley ST, Meinhart CD (2010) Recent advances in micro-particle image velocimetry. Annu Rev Fluid Mech 42:557–576

Westerweel J (1997) Fundamentals of digital particle image velocimetry. Meas Sci Technol 8:1392–1397

White FM (2006) Viscous fluid flow 3rd edn. McGraw-Hill, New York

Xiong R, Bai M, Chung JN (2007) Formation of bubbles in a simple co-flowing micro-channel. J Micromech Microeng 17:1002–1011

Xu JH, Li SW, Chen GG, Luo GS (2006) Formation of monodisperse microbubbles in a microfluidic device. AlChE J 52:2254–2259

Yan D, Nguyen NT, Yang C, Huang X (2006) Visualizing the transient electroosmotic flow and measuring the zeta potential of microchannels with a micro-PIV technique. J Chem Phys 124: 021103